

# Chiral Index Dependence of the $G^+$ and $G^-$ Raman Modes in Semiconducting Carbon Nanotubes

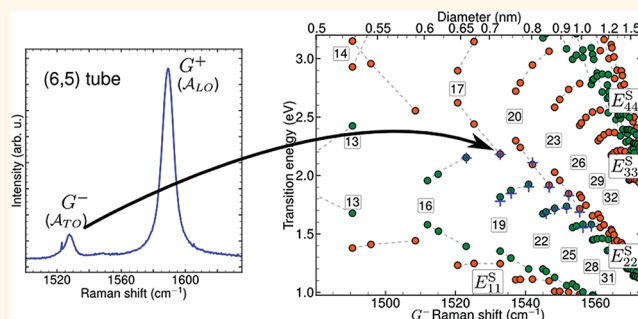
Hagen Telg,<sup>†,\*</sup> Juan G. Duque,<sup>†,||</sup> Matthias Staiger,<sup>‡</sup> Xiaomin Tu,<sup>§</sup> Frank Henrich,<sup>⊥</sup> Manfred M. Kappes,<sup>⊥</sup> Ming Zheng,<sup>§</sup> Janina Maultzsch,<sup>‡</sup> Christian Thomsen,<sup>‡</sup> and Stephen K. Doorn<sup>\*,†</sup>

<sup>†</sup>Center for Integrated Nanotechnologies, Los Alamos National Laboratory, Los Alamos, New Mexico 87545, United States, <sup>‡</sup>Institut für Festkörperphysik, Technische Universität Berlin, Hardenbergstraße 36, 10623 Berlin, Germany, <sup>§</sup>Polymers Division, National Institute of Standards and Technology, 100 Bureau Drive, Stop 8540, Gaithersburg, Maryland 20899-8540, United States, <sup>⊥</sup>Institut für Nanotechnologie, Karlsruher Institut für Technologie, D-76021 Karlsruhe, Germany, and <sup>||</sup>Chemistry Division, Physical Chemistry and Applied Spectroscopy (C-PCS), Los Alamos National Laboratory, Los Alamos, New Mexico 87545, United States

Raman spectroscopy is an established tool to assign the diameter and even the chiral indices  $(n,m)$  of single-wall carbon nanotubes (SWCNTs). Tube diameters are commonly calculated from measured radial breathing mode (RBM) frequencies.<sup>1</sup> If additionally the excitation energy of the irradiating laser is considered, the chiral index of a nanotube giving rise to a particular RBM can be assigned or at least narrowed to a small set of possible  $(n,m)$  candidates.<sup>2–5</sup>

A further prominent feature in the nanotube Raman spectrum is the high-energy  $G$  modes ( $\approx 1540$ – $1595$   $\text{cm}^{-1}$ ). These modes are related to the graphite  $\mathcal{E}_{2g}$  phonon, an optical in-plane vibration.<sup>6</sup> While in graphite the longitudinal and the transverse optical phonons are equivalent at the  $\Gamma$  point and therefore give rise to only one mode in the Raman spectrum, in nanotubes this mode is split into two, the  $G^+$  and  $G^-$  modes. The dominant reason for the splitting is the curvature of the tube wall, which causes a rehybridization of the carbon valence orbitals from  $sp^2$  (planar graphene) to  $sp^3$ -like.<sup>7–9</sup>  $sp^3$  orbitals form significantly weaker bonds than  $sp^2$  orbitals, which leads to softening of the associated Raman peaks. The softening is more pronounced in phonons associated with atomic displacements perpendicular to the tube axis; thus the transverse optical ( $\mathcal{A}_{TO}$ ) phonon. The longitudinal optical ( $\mathcal{A}_{LO}$ ) phonon is dominated by displacements parallel to the tube axis, which are less weakened by the rehybridization and therefore yield a much smaller softening of the phonon. In addition, the phonon frequencies in nanotubes are affected by confinement. The confinement limits the number of electronic states that affect the electron–phonon coupling. This, in turn, has an impact on the

## ABSTRACT



Raman spectroscopy on the radial breathing mode is a common tool to determine the diameter  $d$  or chiral indices  $(n,m)$  of single-wall carbon nanotubes. In this work we present an alternative technique to determine  $d$  and  $(n,m)$  based on the high-energy  $G^-$  mode. From resonant Raman scattering experiments on 14 highly purified single chirality  $(n,m)$  samples we obtain the diameter, chiral angle, and family dependence of the  $G^-$  and  $G^+$  peak position. Considering theoretical predictions we discuss the origin of these dependences with respect to rehybridization of the carbon orbitals, confinement, and electron–electron interactions. The relative Raman intensities of the two peaks have a systematic chiral angle dependence in agreement with theories considering the symmetry of nanotubes and the associated phonons.

**KEYWORDS:** single-wall carbon nanotubes · Raman spectroscopy ·  $G$  mode · LO/TO phonons · diameter determination ·  $(n,m)$  assignment

phonon frequency. For nanotubes the confinement yields an upshift of the  $\mathcal{A}_{LO}$  phonon, while the  $\mathcal{A}_{TO}$  phonon is unaffected.<sup>10</sup> In the Raman spectrum of semiconducting nanotubes the  $\mathcal{A}_{LO}$  and  $\mathcal{A}_{TO}$  phonons are the origin of the  $G^+$  and  $G^-$  peaks, respectively. Note that the discussion above is valid only for semiconducting nanotubes, and all results presented in this paper are exclusively from semiconducting tubes. The  $G$  modes in metallic nanotubes are predicted to also show a diameter dependence for the same reason as in semiconducting nanotubes.

\* Address correspondence to hagen@lanl.gov; skdoorn@lanl.gov.

Received for review November 15, 2011 and accepted December 18, 2011.

Published online December 18, 2011  
10.1021/nn2044356

© 2011 American Chemical Society

However, the phonons are further affected by the Kohn anomaly.<sup>10–12</sup>

Due to an increasing rehybridization, the  $\mathcal{A}_{TO}$  frequency, thus the  $G^-$  position, is expected to decrease strongly with decreasing nanotube diameter.<sup>11,13</sup> This makes the  $G^-$  position an alternative measure for the tube diameter or even a way to perform an  $(n,m)$  assignment. One advantage of the  $G^-$  peak over the RBM is its much wider resonance window, which makes it more likely to obtain a signal from a particular nanotube when a limited number of excitation energies are available.<sup>14,15</sup> So far experimental data of  $G^-$  peak position as a function of diameter exist only for tubes with diameters greater than 1.1 nm. In this diameter regime the frequency variation is small, and therefore the uncertainty in a diameter assignment is large.<sup>16,17</sup> However, in nanotube research there is a broad interest in smaller nanotubes such as high-pressure carbon monoxide conversion (HiPco) or cobalt–molybdenum catalytic procedure (CoMoCat) tubes with a diameter distribution down to 0.6 nm. For these nanotubes a strong diameter dependence of the  $G^-$  peak can be expected, which makes the  $G^-$  peak a promising measure for the tube diameter.

Here we present resonant Raman studies on the diameter, chiral angle, and family dependence of the high-energy modes,  $G^-$  and  $G^+$ , in small-diameter semiconducting SWCNTs suspended in solution. We studied 14 different samples each enriched in nanotubes of one particular chirality  $(n,m)$  in a diameter range between 0.68 and 1.09 nm. We find a strong and weak diameter  $d$  dependence of the  $G^-$  and  $G^+$  peak positions, respectively. Both frequencies decrease with decreasing diameter proportional to  $1/d^2$ . In the large-diameter regime, however, the  $G^+$  peak shows an initial increase that is proportional to  $1/d$ . For the first time we can show that both the  $G^-$  and  $G^+$  frequencies depend on chiral angle, but with opposite sign. Additionally, we find a dependence of the  $G^-$  peak position on the nanotube family. By comparison of our results to theoretical predictions we attribute the  $1/d^2$  and chiral angle dependences to the curvature of the tube wall and the associated rehybridization of the carbon orbitals. The origin of the additional  $1/d$  dependence of the  $G^+$  peak and the family dependence of the  $G^-$  peak are assigned to confinement effects.

To describe the  $G^-$  family dependence, electron–electron interactions must be considered also. Furthermore we find the  $I(G^-)/I(G^+)$  intensity ratio to be maximum for large chiral angle tubes and zero for zero chiral angle, in agreement with symmetry considerations and as shown in the independently index identified work of Michel *et al.*<sup>18</sup> We observe a gradual variation of the ratio between the two extremes and a decrease with increasing diameter. In the last section of this work we show how the result on the diameter dependence of the  $G^-$  peak can be used to determine

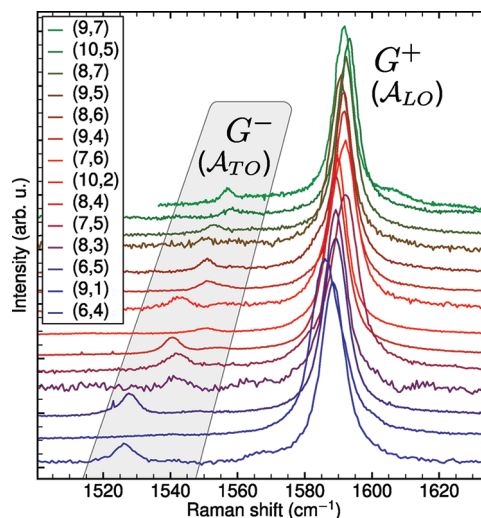


**Figure 1.** High-energy-mode Raman spectra taken with excitation at the optical transition energy for each  $(n,m)$  nanotube in which the sample is enriched. All spectra show a  $G^+$  peak at  $\sim 1590$   $\text{cm}^{-1}$ . The  $G^-$  peak is the much smaller and strongly diameter dependent feature on the low-energy side of the  $G^+$  peak. Tube diameters increase from bottom to top. Intensities are normalized to the intensity of the  $G^+$  peak.

the diameters and even the chiral indices  $(n,m)$  of isolated carbon nanotubes and tubes in mixed chirality samples.

## RESULTS AND DISCUSSION

Raman spectroscopy was performed on 14 separate samples of semiconducting SWCNTs, each enriched in one particular type of nanotube: (9,7), (10,5), (8,7), (9,5), (8,6), (9,4), (7,6), (10,2), (8,4), (7,5), (8,3), (6,5), (9,1), and (6,4). All samples (except the (9,7)) are nanotubes purified by DNA-assisted ion-exchange chromatography as described in ref 19 and then dialyzed into aqueous 1% deoxycholate solution. The (9,7) sample was purified using a selective polymer wrapping technique.<sup>20</sup> An evaluation of sample purity as established by luminescence, absorbance, and Raman spectroscopy can be found in ref 15, which presents results from the identical samples as used here. We note the defect-induced Raman mode was not observed in any of the samples.

Figure 1 shows the high-energy mode Raman spectra of all 14 chirality-enriched samples excited resonantly with the second optical transition  $E_{22}^S$ . Each spectrum shows the characteristic high-energy mode features of carbon nanotubes, a strong  $G^+$  peak near  $1590$   $\text{cm}^{-1}$  and a weak  $G^-$  peak on the low-energy side of  $G^+$ . The diameter of the tubes corresponding to the spectra in Figure 1 increases from bottom to top. The plot shows how the  $G^-$  peak strongly shifts to higher frequencies for larger diameter tubes. We also observe a weak upshift in  $G^+$  frequency as the diameter increases. Superimposed on these trends, the position of both peaks seems to have a random

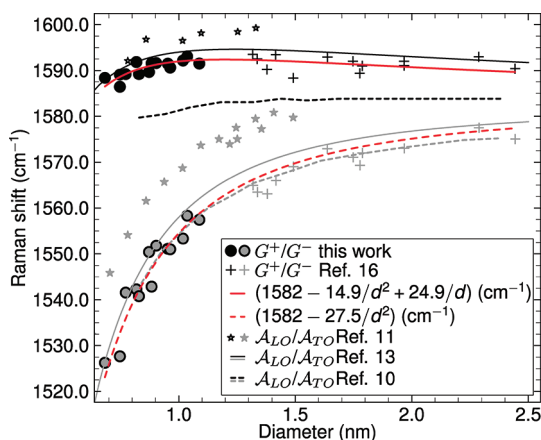


**Figure 2.**  $G^+$  and  $G^-$  frequencies as a function of tube diameter. Solid and dashed red lines represent fits of eq 1 to the combined data from this work (circles) and ref 16 (plus symbols). Black and gray stars and solid and dashed lines are theoretical predictions based on *ab initio*, non-orthogonal tight-binding, and *ab initio* on graphene plus zone-folding approximations, respectively.

**TABLE 1.** Summary of the Studied Nanotube Chiralities ( $n,m$ ) Ordered by Diameter<sup>a</sup>

( $n,m$ )	$\nu$	$\ell$	$d$ (nm)	$\theta$ (deg)	$E_i$ (eV)	$G^+$ ( $\text{cm}^{-1}$ )	$G^-$ ( $\text{cm}^{-1}$ )
(9,7)	-1	25	1.088	25.87	1.559	1591.5	1557.4
(10,5)	-1	25	1.036	19.11	1.569	1593.1	1558.3
(8,7)	1	23	1.018	27.8	1.698	1592.2	1553.3
(9,5)	1	23	0.9626	20.63	1.831	1590.6	1551.0
(8,6)	-1	22	0.953	25.28	1.722	1591.5	1551.1
(9,4)	-1	22	0.9034	17.48	1.710	1591.6	1551.8
(7,6)	1	20	0.8828	27.46	1.907	1591.6	1542.9
(10,2)	-1	22	0.8723	8.948	1.675	1589.7	1550.4
(8,4)	1	20	0.829	19.11	2.101	1589.2	1540.8
(7,5)	-1	19	0.8179	24.5	1.907	1591.8	1542.3
(8,3)	-1	19	0.772	15.3	2.049 <sup>b</sup>	1589.2	1541.6
(6,5)	1	17	0.7473	27.0	2.187	1589.1	1527.7
(9,1)	-1	19	0.7473	5.209	1.759	1586.4	
(6,4)	-1	16	0.683	23.4	2.138	1588.4	1526.3

<sup>a</sup> Nanotube family index,  $\nu = [(n - m) \bmod 3]$ , branch index,  $\ell = 2n + m$ , diameter,  $d = a_0/\pi(n^2 + nm + m^2)^{1/2}$ , and chiral angle,  $\theta = \arccos((n + m/2)/(n^2 + nm + m^2)^{1/2})$ , are given with  $a_0 = 0.246$  nm being the in-plane lattice constant of graphite.<sup>21</sup>  $E_i$  is the used excitation energy. The experimental error of the observed  $G^-$  and  $G^+$  peak positions is  $\pm 1$   $\text{cm}^{-1}$ .<sup>b</sup> This energy matches the outgoing resonance ( $E_{ii} + E_{\text{phonon}}$ ).

shift, which, however, is larger than the experimental uncertainty of  $\pm 1$   $\text{cm}^{-1}$ . In order to discuss the structure dependence of the peak positions, we plot in Figure 2 their frequency as a function of nanotube diameter (gray and black solid circles). The discussed diameter dependence and the apparently random variations of the  $G^-$  and  $G^+$  peak positions become even more apparent in this plot. G-band peak positions for the 14 chiralities measured here are given in Table 1.

**Frequency Dependence on Diameter.** We focus first on the observed diameter dependence of  $G^-$  and  $G^+$ , neglecting other influences such as chiral angle or nanotube family. To extend the resulting diameter

**TABLE 2.** Results from Fitting eq 1 to Data Presented in the Particular References<sup>a</sup>

	ref	$a_0$ ( $\text{cm}^{-1}$ )	$a_1$	$a_2$
$G^+/\mathcal{L}_{10}$	this work + Paillet <i>et al.</i> <sup>16</sup>	1582	-14.9	24.9
	Jorio <i>et al.</i> <sup>17</sup> (exptl)	1591	0	0
	Dubay <i>et al.</i> <sup>11</sup> (theor)	1593	-13.2	17.6
$G^-/\mathcal{L}_{10}$	Popov <i>et al.</i> <sup>13</sup> (theor)	1582	-20.8	31.5
	this work + Paillet <i>et al.</i> <sup>16</sup>	1582	-27.5	0
	Jorio <i>et al.</i> <sup>17</sup> (exptl)	1591	-47.7	0
$G^-/\mathcal{L}_{10}$	Dubay <i>et al.</i> <sup>11</sup> (theor)	1591	-22.9	0
	Popov <i>et al.</i> <sup>13</sup> (theor)	1582	-22.0	0

<sup>a</sup> Data from this work was fit after combining it to results for larger diameter tubes taken from ref 16.

dependence to larger diameters, we add experimental data from Paillet (plus symbols) to our results in Figure 2.<sup>16</sup> They present results on  $G^-$  and  $G^+$  from CVD (chemical vapor deposition)-grown semiconducting nanotubes that are suspended across trenches. The RBM in carbon nanotubes is known to have some dependence on the tube environment.<sup>4,22</sup> However, the RBM is an out-of-plane vibration that can be assumed to be more affected than the in-plane vibrations associated with the  $G^-$  and  $G^+$  peaks. Thus, we neglect such effects on the  $G^-$  and  $G^+$  mode frequencies here.

We find that the combined data sets are fit well by eq 1, with the resulting fits for  $G^-$  and  $G^+$  shown in Figure 2 as a solid and dashed red line, respectively, with best fit values for the coefficients  $a_n$  given in Figure 2.

$$\omega_{\text{ph}}(d) = a_0 + \frac{a_1}{d^2} + \frac{a_2}{d} \quad (1)$$

Assuming the frequencies of both the  $G^-$  and  $G^+$  peaks approach with increasing diameter the value of the  $\mathcal{G}_{2g}$  mode in graphite and graphene, respectively, we fixed the value  $a_0$  to 1582  $\text{cm}^{-1}$ .<sup>6,23</sup> The second term,  $a_1/d^2$ , describes the strong decrease of both peaks for small-diameter nanotubes. The third term in eq 1,  $a_2/d$ , accounts for the fact that the frequency of the  $G^+$  initially increases with decreasing diameter before it decreases again for very small diameter tubes. It has been shown that simulating confinement by applying zone-folding to a graphene sheet results in an upshift of the  $\mathcal{L}_{10}$  frequencies with decreasing diameter that is proportional to  $1/d$ .<sup>10</sup> Therefore the third term in eq 1 can be associated with confinement, while the second term results from the curvature of the tube wall. In the case of the  $G^-$  peak the monotonic decrease of the frequency with diameter is well described by the first two terms, making the third term unnecessary. Hence, for  $G^-$   $a_2$  is zero.

In addition to the experimental data, we also give in Figure 2 and Table 2 theoretical predictions for the diameter dependence of the  $\mathcal{L}_{10}$  and  $\mathcal{L}_{11}$  phonons.<sup>10,11,13</sup> In general each theory describes a functional form that is similar to our result and therefore can all be described by eq 1. Data given by Dubay (stars in Figure 2) result from *ab*

*initio* calculations on zigzag  $((n,m) = (n,0))$  nanotubes.<sup>11</sup> Including the curvature of the tube wall, confinement, and electron–electron interactions, this theory can be considered the most accurate of the theories discussed here. Their predictions tend to overestimate the experimentally observed frequencies, which can be attributed to electron–hole interactions not being included in this theory.<sup>24</sup> However, the deviation is basically an offset reflected in a different value  $a_0$ , while the functional form represented by  $a_1$  and  $a_2$  is close to the experimental values. As we discuss later, these small deviations in  $a_1$  and  $a_2$  can be traced back to variations of the phonon frequency with chiral angle  $\theta$  and the fact that data in ref 11 is solely based on zigzag tubes with  $\theta = 0$ . Predictions by Popov *et al.*<sup>13</sup> are based on a nonorthogonal tight-binding description, a technique that takes the first nearest neighbor into account and considers curvature effects and confinement. Compared to first-principle calculations, this theory has the advantage that it can describe the phonons of nanotubes with any chiral index  $(n,m)$  due to lower computational costs. The gray line in Figure 2 shows the predicted frequencies for nanotubes with  $\theta = 20^\circ$ , which is the average angle of all nanotubes in our study. Besides a small offset for the  $\mathcal{A}_{TO}$  phonons, the predictions reproduce the experimental values very well. But, when considering even smaller diameters than plotted in Figure 1 the difference in  $a_1$  will lead to significant deviations of the  $\mathcal{A}_{LO}$  phonon. The fact that the simple tight-binding description from ref 13 reproduces the experimentally observed diameter dependence shows that, in the diameter range considered here, electron–electron interactions play only a minor role. However, as we will show in the next section, electron–electron interactions must be considered to explain variations of peak positions between the different nanotube families  $\nu = \pm 1$ . Note that we did not include ref 10 in the foregoing discussion since the presented theory is based on graphene without any curvature. The effect of curvature was subsequently estimated on the basis of predictions from the work of Dubay *et al.*<sup>11</sup> It is the combined result that gives the gray and black dashed lines of Figure 2.

Table 2 additionally gives previous experimental results for the diameter dependence of the  $G^-$  and  $G^+$  peaks based on larger diameter ( $d \approx 1.1$ – $2.5$  nm) nanotubes.<sup>17</sup> The strong deviation of their fit parameters from our results is in part due to the adoption of an unreasonably high  $a_0$ . Additionally, at the time ref 17 was published, Raman-based  $(n,m)$  and chiral angle assignments were not yet reliable. Finally, the results of ref 17 do not extend uniformly over the full range of chiral angles, with large chiral angle tubes being over-represented in that data. In the next section we show that the  $G^-$  frequency strongly depends on the chiral angle and that large chiral angle tubes show a stronger diameter dependence than small chiral angle tubes, which could be a further reason for the strong diameter dependence observed in ref 17. These differences

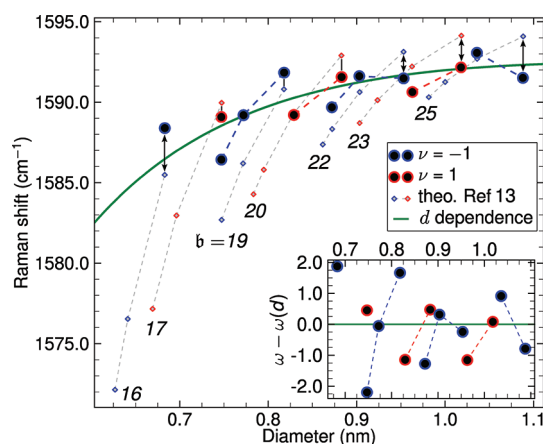


Figure 3.  $G^+$  frequencies as a function of diameter.  $\nu = \pm 1$  indicate the two families of semiconducting nanotubes. Green line: fit to eq 1. Data points of tubes within the same branch  $b$  are connected by dashed lines. Numbers indicate branch index  $b$ . Chiral angle changes within each branch from  $\theta \geq 0$  for smallest diameter tube to  $\theta < 30^\circ$  for the largest diameter tube. Diamonds are data from nonorthogonal tight-binding calculations from ref 13. Data points that correspond to the same tube in exptl and theor have matching diameters (see arrows for near-armchair tubes). Inset: Frequencies subtracted by the overall diameter dependence of eq 1.

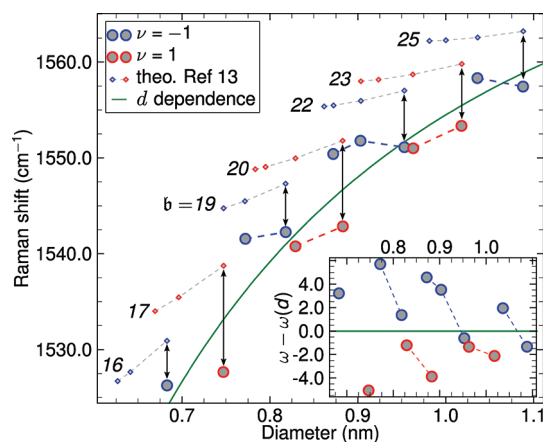


Figure 4.  $G^-$  frequencies as a function of diameter. For more details see caption of Figure 3.

underscore the importance of considering a larger range of structures that extends to much smaller diameters and that includes the full range of available chiral angles, allowing an accounting of effects not considered in ref 17.

**Frequency Dependence on Chiral Angle and Family.** The obtained diameter dependence of the  $G^-$  peak as described above can in principle be used to determine the diameter of nanotubes from measured  $G^-$  frequencies. However, data points are found to deviate by up to  $\pm 4$   $\text{cm}^{-1}$  from the fit result, which adds a significant uncertainty of  $\pm 0.05$  nm (at 0.9 nm) to a diameter determined this way. Since this deviation is larger than the experimental error in our measurements ( $\pm 1$  cm), a frequency dependence on additional parameters (including chiral angle and family) is suggested.

We show the peak position of  $G^+$  (Figure 3) and  $G^-$  (Figure 4) as a function of diameter. To highlight variations that depend on the chiral angle, we connect tubes of the same branch  $\ell$ ,  $\ell = 2n + m$ , with a dashed line. Within a branch the chiral angle  $\theta$  changes with increasing diameter from  $\theta \approx 0^\circ$  to  $\theta \approx 30^\circ$ . Tubes of the different nanotube families  $\nu = \pm 1$  are given by blue circles ( $\nu = -1$ ) and red circles ( $\nu = +1$ ). The frequencies of the  $G^+$  as well as the  $G^-$  show similar branch patterns, indicating the presence of a chiral angle dependence. However, with respect to the overall diameter dependence, the slope of the chiral angle dependence is positive for the  $G^+$  peak, while it is negative for the  $G^-$  peak. These trends become more apparent when the diameter dependence of the frequencies is factored out by subtracting the trend of eq 1 from the experimental frequencies; see insets to Figure 3 and Figure 4. For the  $G^+$  peak (Figure 3) we see the difference  $\omega - \omega(d)$  between the observed peak position  $\omega$  and the overall diameter dependence  $\omega(d)$  to increase with increasing chiral angle. For the  $G^-$  peak this trend is reversed.

The data also show that the chiral angle dependence increases with decreasing tube diameter. The dependence on chiral angle can be understood by considering the symmetry of the  $\pi$  and  $\sigma$  orbitals. While in armchair tubes  $[(n,n) \rightarrow \theta = 30^\circ]$  some of the  $\sigma$  bonds are parallel to the circumference, none of the bonds are in zigzag tubes  $[(n,0) \rightarrow \theta = 0^\circ]$ . Considering the curved tube wall,  $\sigma$  bonds that are parallel to the circumference will show a larger overlap with the  $\pi$  bonds and therefore form a more pronounced rehybridized orbital. The rehybridized bond is weaker than the initial state and therefore results in a softened  $\mathcal{A}_{\text{TO}}$  phonon. Therefore, the weakening of the  $\mathcal{A}_{\text{TO}}$  phonon gradually increases when the chiral angle changes from  $\theta = 0^\circ$  to  $\theta = 30^\circ$ . For the same reason the  $\mathcal{A}_{\text{LO}}$  phonon shows a gradual weakening when  $\theta$  changes from  $\theta = 30^\circ$  to  $\theta = 0^\circ$ . The effect of rehybridization on the phonon frequencies in carbon nanotubes was previously observed on the RBM, where the softening is more pronounced in zigzag ( $\theta = 0^\circ$ ) than in armchair ( $\theta = 30^\circ$ ) tubes, similar to the behavior of the  $G^+$  mode reported here.<sup>4,25</sup> Furthermore we observe a family dependence of the  $G^-$  frequencies. The inset in Figure 4 shows that most  $G^-$  frequencies of tubes with  $\nu = -1$  ( $\nu = +1$ ) lie above (below) the overall diameter dependence. A similar trend is not observed for the  $G^+$  peak (see inset in Figure 3).

In addition to our experimental results we plot in Figure 3 and Figure 4 theoretical predictions from non-orthogonal tight-binding approximations.<sup>13</sup> For ease of comparison, the points for near-armchair experimental values are connected to the corresponding theoretical values by vertical arrows. Keeping in mind that the slope of each branch with diameter represents the chiral angle dependence of the G-band frequencies, the theoretical predictions are in good agreement with our experimental results. In particular, the theory reproduces the trend that

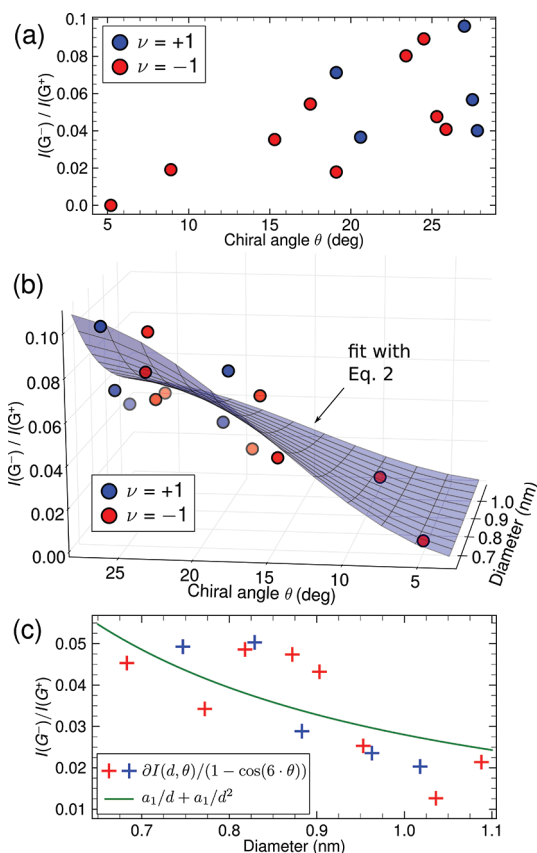


**Figure 5.** (a) Ratio of  $G^-$  and  $G^+$  intensities ( $I(G^-)/I(G^+)$ ) as a function of chiral angle  $\theta$ . (b)  $I(G^-)/I(G^+)$  as a function of  $\theta$  and diameter. (c) Data (plus symbols) and fit result (green line) normalized to the chiral angle dependence as defined in eq 2.

the chiral angle dependence increases as diameter decreases. However, a quantitative comparison to the experimental findings shows that the theory overestimates the slope of the chiral angle dependence, especially in the case of the  $\mathcal{A}_{\text{LO}}$  phonon. Furthermore, the family dependence observed for the  $G^-$  peak is not described by the theoretical data in ref 13. To explain the family dependence, we consider instead the work of Piscanec *et al.*<sup>10</sup> In their section D.1 they show results from density functional theory on flat graphene, whose 2D reciprocal space is constrained to lines according to the particular nanotube chiral indices  $(n,m)$  by applying zone-folding. Therefore the theory accounts for electron–electron interactions and confinement but neglects the curvature of the nanotube wall. Results on the  $\mathcal{A}_{\text{LO}}$  and  $\mathcal{A}_{\text{TO}}$  phonons in semiconducting nanotubes show no dependence on the nanotube chiral angle but reveal a family dependence for the  $\mathcal{A}_{\text{TO}}$  phonon (Figure 8 in ref 10). They predict the  $\mathcal{A}_{\text{TO}}$  phonon to be higher for tubes with  $\nu = -1$  compared to tubes with  $\nu = +1$ , in agreement with our experimental findings.

In conclusion, the chiral angle dependence of the  $G^-$  and  $G^+$  peak positions is well described by the  $\mathcal{A}_{\text{LO}}$  and  $\mathcal{A}_{\text{TO}}$  frequencies obtained from a nonorthogonal tight binding approximation, which accounts for confinement and curvature but neglects electron–electron interactions.

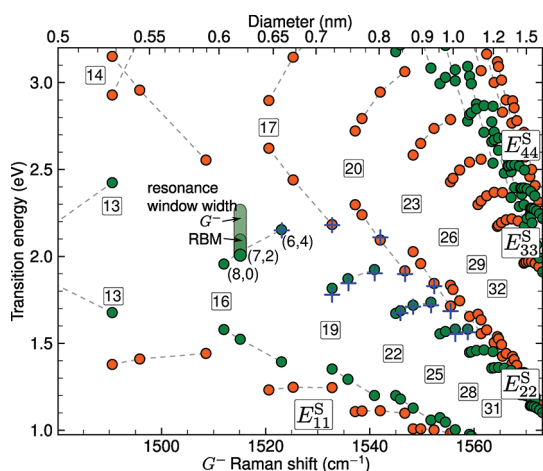


**Figure 6.** Correlation of  $G^-$  frequency and transition energy  $E_{ii}$  for a particular nanotube  $(n,m)$  for the first four optical transitions of semiconducting tubes. Circles: data taken from ref 32, where the diameter was transferred to Raman shift using eq 1. Green (red) circles indicate tubes with  $\nu = -1$  ( $\nu = +1$ ). Numbers give branch  $\ell$  indices for next branch above as well as below number. Plus symbols: results from this work.

However, this theory fails to describe the family dependence of the  $G^-$  frequencies. On the other hand, a combined zone-folding and DFT approach that accounts for electron–electron interactions and confinement, but neglects curvature, does not predict a chiral angle dependence but predicts the experimentally observed family dependence. Therefore the chiral angle dependence is dominated by the curvature of the wall, while the family dependence results from a combination of confinement and electron–electron interactions.

**$G^-/G^+$  Intensity Ratio.** In the following section we discuss results on the observed  $G^-$  and  $G^+$  peak intensities. Further inspection of the Raman spectra in Figure 1 makes apparent that the intensity of the  $G^-$  peak relative to the  $G^+$  varies for different samples. The fact that the two smallest chiral angle tubes, (9,1) and (10,2), show the weakest  $G^-$  intensity establishes that the  $G^-$  intensity depends on chiral angle. Since we are not able to determine the accurate concentration of nanotubes in our samples, we studied the ratio  $\partial I = I(G^-)/I(G^+)$  between the intensities of the two peaks. Figure 5a shows  $\partial I$  as a function of chiral angle. The plot shows a general trend of a decreasing intensity ratio for smaller chiral angles, but with significant scatter introduced at specific values due to an overlapping diameter dependence. Figure 5b shows  $\partial I$  as a function of chiral angle and diameter. The plot reveals the convolution of a decrease of  $\partial I$  with chiral angle and a decrease of  $\partial I$  with increasing diameter. The surface shown in Figure 5b is the result of fitting eq 2 to the data where  $b_1 = 0.014$  nm and  $b_2 = 0.014$  nm<sup>2</sup>.

$$\partial I(d, \theta) = \frac{I(G^-)}{I(G^+)} = \left( \frac{b_1}{d} + \frac{b_2}{d^2} \right) (1 - \cos(6\theta)) \quad (2)$$

Normalizing the observed  $\partial I$  to the chiral angle dependence described by the last term in eq 2 ( $(1 - \cos(6\theta))$ )

reveals the diameter dependence of  $\partial I$ , given by the plus symbols in Figure 5c.

The dependence on the chiral angle can be derived from the symmetry of nanotubes, which predicts only the  $\mathcal{A}_{TO}$  phonon to be Raman allowed in armchair tubes ( $\theta = 30^\circ$ ).<sup>18,26–29</sup> In zigzag tubes ( $\theta = 0^\circ$ ) only the  $\mathcal{A}_{LO}$  phonon is predicted to be observable in a Raman experiment. The gradual increase of  $\partial I$  for increasing chiral angle as well as the decrease with increasing diameter is in good agreement with theoretical predictions based on tight-binding approximations.<sup>30,31</sup> When comparing our results to the experimental results on freely suspended nanotubes presented in ref 18, we find a difference in intensity ratio of almost an order of magnitude. This difference might be an effect from the different environment. However, considering the good agreement between our results and theory suggests that results from ref 18 are not showing the intrinsic Raman intensities, possibly due to damage introduced by the etching process used in ref 18 for sample preparation.

The result on an increasing  $\partial I$  with increasing chiral angle can be used as a support for  $(n,m)$  assignments as shown in ref 27.

**$(n,m)$  Assignment.** In this last section we show how the observed diameter dependence of  $G^-$  on the peak position can be used to assign the chiral indices  $(n,m)$  of nanotubes present in a sample. Similar to the technique based on the RBM widely used in the literature, the assignment we present here is based on the so-called Kataura plot.<sup>2–5</sup> In this plot the transition energies of each nanotube are plotted as a function of diameter, which results in a characteristic pattern. In order to use such a plot for a  $(n,m)$  assignment, it is necessary to find an experimentally addressable nanotube property that is diameter dependent and is only observable when excitation is in resonance with one of the nanotube's optical transitions. As an alternative to the RBM, we show here that at least for small-diameter nanotubes ( $\leq 1$  nm) the diameter dependence of the  $G^-$  mode is suitable to perform a  $(n,m)$  assignment.

In Figure 6 we show an empirical Kataura plot in which transition energies are taken from ref 32 and the diameter has been translated to the  $G^-$  frequency using eq 1 with  $a_0 = 1582$  cm<sup>-1</sup> and  $a_1 = -27.5$  nm<sup>2</sup>/cm (from Table 2). The corresponding diameters are given in the top abscissa. The resulting plot shows the characteristic Kataura plot pattern of bands representing optical transitions ( $E_{11}^S$ ,  $E_{22}^S$ ,  $E_{33}^S$ : first, second, and third transitions of semiconducting tubes) and branches that bend away from these bands.

To find the chiral index of the nanotube referring to a particular data point, one takes the branch index  $\ell$  ( $\ell = 2n + m$ ) and divides it by 2. The chiral index of the tube with the smallest diameter within a branch is given by the quotient, while the remainder defines  $m$ . The neighboring tube with larger diameter within the same branch is given by  $(n - 1, m + 2)$ . In order to assign

a particular nanotube ( $n,m$ ) to an observed  $G^-$  peak, one takes the  $G^-$  peak position and the excitation energy at which the peak was observed and adds it to the plot shown in Figure 6. This new data point should coincide with a point already existing in Figure 6 and which can therefore be related to a particular nanotube chiral index ( $n,m$ ). Note that the Raman signal can be observed when exciting with energies within the resonance window ( $\approx$ phonon energy plus electronic line width). In case of the  $G^-$  mode this window has a width of roughly 260 meV, as illustrated for the (7,2) tube in Figure 6. If ambiguities occur, the consultation of Raman intensities as described in the previous section can help in finding an unambiguous assignment. In addition to the empirical data, Figure 6 shows the measured results from this work (plus symbols). As expected each plus sign coincides very well with a data point of the empirical plot and therefore can be easily assigned to a particular ( $n,m$ ).

We note that the Raman shift in the empirical data is solely obtained from the diameter dependence of the  $G^-$  peak (eq 1) and does not consider variation with chiral angle. However, the agreement between the empirical plot and the findings from this work is unambiguous. Our results suggest an increase of the chiral angle dependence for smaller diameters and, thus, an increase in deviations between experimental data and the empirical data. However, since distances between data points in Figure 6 constantly increase for smaller diameters, these deviations will not affect any assignments.

The described assignment is very similar to assignments based on the radial breathing mode.<sup>4</sup> However, using the  $G^-$  peak instead of the RBM has significant advantages as well as some disadvantages. One major advantage is the larger resonance window, which is more than twice as large for the  $G^-$  mode compared to the RBM (see illustration in Figure 6). This means that in order to obtain a signal of a particular nanotube the laser line, which in many Raman systems is fixed to particular energies, can match the transition energy of that nanotube less accurately in the case of the  $G^-$  peak compared to the RBM peak. However, the wide resonance can lead to ambiguous assignments for diameters above  $\sim 0.8$  nm due to spectral overlap. Furthermore, a  $G^-$ -based assignment offers an alternative whenever a RBM-based assignment is uncertain or the RBM cannot be observed, *e.g.*, when it is cut off by Rayleigh light filters, spectrally contaminated, or simply not present due to a weak electron–phonon coupling.<sup>33</sup> A disadvantage of using the  $G^-$  peak over using the RBM for a ( $n,m$ ) assignment is the fact that the

position of the  $G^-$  peak has a diameter dependence that goes with  $1/d^2$ , while the RBM has a  $1/d$  relation. Therefore, as the diameter increases, the  $G^-$  peak approaches more rapidly a regime where the signal from two tubes can no longer be resolved as separate peaks. The data points in Figure 6 have a diameter of  $\sim 2.5$  nm (half the full width at half-maximum of the  $G^-$  peak). Therefore, as data points overlap, assignments become more difficult.

The chiral angle dependence of the Raman intensity of the  $G^-$  mode also introduces advantages and difficulties for ( $n,m$ ) assignments. On one hand, little signal is observed for very small chiral angles, which makes the  $G^-$  peak problematic for their assignment. On the other hand, the RBM electron–phonon coupling is known to be very weak for large chiral angles at certain transitions  $E_{ij}$  and family  $\nu$ .<sup>33</sup> Because we do not observe a similar family dependence for the  $G^-$  peak, it can substitute for an ( $n,m$ ) assignment when the RBM fails. A further issue regarding the quality of an ( $n,m$ ) assignment is the sample type. Nanotube ensembles containing many different types of nanotubes ( $n,m$ ) are more prone to spectral overlap than single-tube experiments. In nanotube ensembles the  $G^+$  peak will most certainly reflect the accumulated signal from many ( $n,m$ ), which makes the  $G^-/G^+$  intensity ratio unreliable as a tool to narrow down an assignment, while it is certainly useful for single tubes.<sup>27</sup>

## CONCLUSION

In conclusion, we present the  $G^-$  and  $G^+$  mode Raman frequencies of 14 different small-diameter ( $d < 1.1$  nm) semiconducting nanotubes. We find the Raman shift of both peaks decreases as  $1/d^2$  with decreasing diameter as a result of the curvature and the associated rehybridization of the carbon orbitals. The observed diameter dependence of the  $G^-$  peak is sufficient to allow its use in determining the diameter of small nanotubes using  $\omega_{G^-}(d) = a_0 + a_1/d^2$  with  $a_0 = 1582$  cm<sup>-1</sup> and  $a_1 = -27.5$  nm<sup>2</sup>/cm. In addition we find both peak positions to depend on chiral angle, also attributed to the rehybridization. A family dependence results from a combination of confinement and electron–electron interactions. The observed intensities of the  $G^-$  peaks show their predicted absence for chiral angles close or equal to zero degrees and steadily increase with increasing angle. On the basis of the diameter dependence of the  $G^-$  mode we present a technique to assign the chiral indices ( $n,m$ ) of small-diameter carbon nanotubes ( $d \lesssim 1$  nm).

## METHODS

Resonant Raman measurements were performed on the nanotube solutions in backscattering geometry on a triple-

monochromator system paired with a charge-coupled device detector. To ensure that the observed features in the Raman spectrum can be assigned to the particular enriched nanotube

chirality ( $n,m$ ). we tuned the laser energy to match the corresponding transition energy of the second optical transition. Dye lasers using Rhodamine 6G and Kyton red and a titanium-sapphire laser were used as tunable excitation sources. Frequencies were calibrated using Raman peaks of Tylenol and benzonitrile. Spectra were acquired with 5 min integration times, while keeping the laser power at 20 mW.

**Acknowledgment.** H.T, J.G.D., and S.K.D. acknowledge support of the U.S. Department of Energy through the LANL-LDRD program. X.T. and M.Z. acknowledge the support of NSF Grant CMS-060950. J.M. acknowledges support from the European Research Council, ERC grant no. 259286. F.H. and M.K. acknowledge support by the DFG-funded Center for Functional Nanostructures (CFN) and by the Helmholtz Association. This work was performed in part at the Center for Integrated Nanotechnologies, a U.S. Department of Energy, Office of Basic Energy Sciences, user facility.

## REFERENCES AND NOTES

- Reich, S.; Thomsen, C.; Maultzsch, J. *Carbon Nanotubes: Basic Concepts and Physical Properties*; Wiley-VCH: Berlin, 2004.
- Telg, H.; Maultzsch, J.; Reich, S.; Hennrich, F.; Thomsen, C. Chirality Distribution and Transition Energies of Carbon Nanotubes. *Phys. Rev. Lett.* **2004**, *93*, 177401.
- Fantini, C.; Jorio, A.; Souza, M.; Strano, M.; Dresselhaus, M.; Pimenta, M. Optical Transition Energies for Carbon Nanotubes from Resonant Raman Spectroscopy: Environment and Temperature Effects. *Phys. Rev. Lett.* **2004**, *93*, 147406.
- Maultzsch, J.; Telg, H.; Reich, S.; Thomsen, C. Radial Breathing Mode of Single-Walled Carbon Nanotubes: Optical Transition Energies and Chiral-Index Assignment. *Phys. Rev. B* **2005**, *72*, 205438.
- Doorn, S. K.; Heller, D.; Barone, P.; Usrey, M.; Strano, M. Resonant Raman Excitation Profiles of Individually Dispersed Single Walled Carbon Nanotubes in Solution. *Appl. Phys. A: Mater. Sci. Processes* **2004**, *78*, 1147–1155.
- Reich, S.; Thomsen, C. Raman Spectroscopy of Graphite. *Phil. Trans. R. Soc. London A* **2004**, *362*, 2271–2288.
- Blase, X.; Benedict, L.; Shirley, E.; Louie, S. Hybridization Effects and Metallicity in Small Radius Carbon Nanotubes. *Phys. Rev. Lett.* **1994**, *72*, 1878–1881.
- Bacsa, W.; Ugarte, D.; Châtelain, A.; de Heer, W. High-Resolution Electron Microscopy and Inelastic Light Scattering of Purified Multishelled Carbon Nanotubes. *Phys. Rev. B* **1994**, *50*, 15473–15476.
- Sánchez-Portal, D.; Artacho, E.; Soler, J.; Rubio, A.; Ordejón, P. Ab Initio Structural, Elastic, and Vibrational Properties of Carbon Nanotubes. *Phys. Rev. B* **1999**, *59*, 12678–12688.
- Piscanec, S.; Lazzeri, M.; Robertson, J.; Ferrari, A. C.; Mauri, F. Optical Phonons in Carbon Nanotubes: Kohn Anomalies, Peierls Distortions, and Dynamic Effects. *Phys. Rev. B* **2007**, *75*, 35427.
- Dubay, O.; Kresse, G.; Kuzmany, H. Phonon Softening in Metallic Nanotubes by a Peierls-Like Mechanism. *Phys. Rev. Lett.* **2002**, *88*, 235506.
- Lazzeri, M.; Piscanec, S.; Mauri, F.; Ferrari, A. C.; Robertson, J. Phonon Linewidths and Electron-Phonon Coupling in Graphite and Nanotubes. *Phys. Rev. B* **2006**, *73*, 155426.
- Popov, V. N.; Lambin, P. Radius and Chirality Dependence of the Radial Breathing Mode and the G-Band Phonon Modes of Single-Walled Carbon Nanotubes. *Phys. Rev. B* **2006**, *73*, 085407.
- Fouquet, M.; Telg, H.; Maultzsch, J.; Wu, Y.; Chandra, B.; Hone, J.; Heinz, T.; Thomsen, C. Longitudinal Optical Phonons in Metallic and Semiconducting Carbon Nanotubes. *Phys. Rev. Lett.* **2009**, *102*, 075501.
- Duque, J. G.; Chen, H.; Swan, A. K.; Shreve, A. P.; Kilina, S.; Tretiak, S.; Tu, X.; Zheng, M.; Doorn, S. K. Violation of the Condon Approximation in Semiconducting Carbon Nanotubes. *ACS Nano* **2011**, *5*, 5233–5241.
- Paillet, M.; Michel, T.; Meyer, J. C.; Popov, V. N.; Henrard, L.; Roth, S.; Sauvajol, J.-L. Raman Active Phonons of Identified Semiconducting Single-Walled Carbon Nanotubes. *Phys. Rev. Lett.* **2006**, *96*, 257401.
- Jorio, A.; *et al.* G-Band Resonant Raman Study of 62 Isolated Single-Wall Carbon Nanotubes. *Phys. Rev. B* **2002**, *65*, 155412.
- Michel, T.; Paillet, M.; Nakabayashi, D.; Picher, M.; Jourdain, V.; Meyer, J. C.; Zahab, A. A.; Sauvajol, J.-L. Indexing of Individual Single-Walled Carbon Nanotubes from Raman Spectroscopy. *Phys. Rev. B* **2009**, *80*, 245416.
- Tu, X.; Manohar, S.; Jagota, A.; Zheng, M. DNA Sequence Motifs for Structure-Specific Recognition and Separation of Carbon Nanotubes. *Nature* **2009**, *460*, 250–253.
- Nish, A.; Hwang, J.-Y.; Doig, J.; Nicholas, R. J. Highly Selective Dispersion of Single-Walled Carbon Nanotubes Using Aromatic Polymers. *Nat. Nanotechnol.* **2007**, *2*, 640–646.
- Baskin, Y.; Meyer, L. Lattice Constants of Graphite at Low Temperatures. *Phys. Rev.* **1955**, *100*, 544.
- Araujo, P. T.; Jorio, A.; Maciel, I. O.; Pesce, P. B. C.; Doorn, S. K.; Pimenta, M. A.; Qian, H.; Hartschuh, A.; Steiner, M.; Grigorian, L.; *et al.* Nature of the Constant Factor in the Relation Between Radial Breathing Mode Frequency and Tube Diameter for Single-Wall Carbon Nanotubes. *Phys. Rev. B* **2008**, *77*, 241403.
- Berciaud, S.; Ryu, S.; Brus, L. E.; Heinz, T. F. Probing the Intrinsic Properties of Exfoliated Graphene: Raman Spectroscopy of Free-Standing Monolayers. *Nano Lett.* **2009**, *9*, 346–352.
- Lazzeri, M.; Attacalite, C.; Wirtz, L.; Mauri, F. Impact of the Electron-Electron Correlation on Phonon Dispersion: Failure of LDA and GGA DFT Functionals in Graphene and Graphite. *Phys. Rev. B* **2008**, *78*, 081406.
- Jorio, A.; Fantini, C.; Pimenta, M.; Capaz, R.; Samsonidze, G. G.; Dresselhaus, G.; Dresselhaus, M.; Jiang, J.; Kobayashi, N.; Grüneis, A.; *et al.* Resonance Raman Spectroscopy ( $n,m$ )-Dependent Effects in Small-Diameter Single-Wall Carbon Nanotubes. *Phys. Rev. B* **2005**, *71*, 075401.
- Damjanović, M.; Milošević, I.; Vuković, T.; Sredanović, R. Full Symmetry, Optical Activity, and Potentials of Single-Wall and Multiwall Nanotubes. *Phys. Rev. B* **1999**, *60*, 2728–2739.
- Paillet, M.; Michel, T.; Zahab, A.; Nakabayashi, D.; Jourdain, V.; Parret, R.; Meyer, J. C.; Sauvajol, J.-L. Probing the Structure of Single-Walled Carbon Nanotubes by Resonant Raman Scattering. *Phys. Status Solidi B* **2010**, *247*, 2762–2767.
- Berciaud, S.; Voisin, C.; Yan, H.; Chandra, B.; Caldwell, R.; Shan, Y.; Brus, L. E.; Hone, J.; Heinz, T. F. Excitons and High-Order Optical Transitions in Individual Carbon Nanotubes: A Rayleigh Scattering Spectroscopy Study. *Phys. Rev. B* **2010**, *81*, 041414.
- Hároz, E. H.; Duque, J. G.; Rice, W.; Densmore, C.; Kono, J.; Doorn, S. Resonant Raman Spectroscopy of Armchair Carbon Nanotubes: Absence of Broad  $G^-$  Feature. *Phys. Rev. B* **2011**, *84*, 121403.
- Popov, V. N.; Lambin, P. Symmetry-Adapted Tight-Binding Calculations of the Totally Symmetric  $A_1$  Phonons of Single-Walled Carbon Nanotubes and Their Resonant Raman Intensity. *Physica E (Amsterdam, Neth.)* **2007**, *37*, 97–104.
- Saito, R.; Jorio, A.; Hafner, J.; Lieber, C.; Hunter, M.; McClure, T.; Dresselhaus, G.; Dresselhaus, M. Chirality-Dependent G-band Raman Intensity of Carbon Nanotubes. *Phys. Rev. B* **2001**, *64*, 085312.
- Araujo, P.; Doorn, S.; Kilina, S.; Tretiak, S.; Einarsson, E.; Maruyama, S.; Chacham, H.; Pimenta, M.; Jorio, A. Third and Fourth Optical Transitions in Semiconducting Carbon Nanotubes. *Phys. Rev. Lett.* **2007**, *98*, 067401.
- Telg, H.; Thomsen, C.; Maultzsch, J. Raman Intensities of the Radial-Breathing Mode in Carbon Nanotubes: the Exciton-Phonon Coupling as a Function of  $(n_1, n_2)$ . *J. Nanophoton.* **2010**, *4*, 041660.